



Cite this: *Dalton Trans.*, 2016, **45**, 10058

Dynamic ruffling distortion of the heme substrate in non-canonical heme oxygenase enzymes†

Amanda B. Graves, Erik H. Horak and Matthew D. Liptak*

Recent work by several groups has established that MhuD, IsdG, and IsdI are non-canonical heme oxygenases that induce significant out-of-plane ruffling distortions of their heme substrates enroute to mycobilin or staphylobilin formation. However, clear explanations for the observations of “nested” $S = \frac{1}{2}$ VTVH MCD saturation magnetization curves at cryogenic temperatures, and exchange broadened ^1H NMR resonances at physiologically-relevant temperatures have remained elusive. Here, MCD and NMR data have been acquired for F23A and F23W MhuD–heme–CN, in addition to MCD data for IsdI–heme–CN, in order to complete assembly of a library of spectroscopic data for cyanide-inhibited ferric heme with a wide range of ruffling deformations. The spectroscopic data were used to evaluate a number of computational models for cyanide-inhibited ferric heme, which ultimately led to the development of an accurate NEVPT2/CASSCF model. The resulting model has a shallow, double-well potential along the porphyrin ruffling coordinate, which provides clear explanations for the unusual MCD and NMR data. The shallow, double-well potential also implies that MhuD-, IsdG-, and IsdI-bound heme is dynamic, and the functional implications of these dynamics are discussed.

Received 22nd February 2016,

Accepted 28th May 2016

DOI: 10.1039/c6dt00702c

www.rsc.org/dalton

Introduction

Non-canonical heme oxygenases (HOs) are a recently discovered class of enzymes that catalyse novel heme- and oxygen-dependent reactions.¹ These enzymes do not follow the paradigm established for canonical HOs where heme is converted to iron, biliverdin, and carbon monoxide *via meso*-hydroxyheme and verdoheme intermediates.² Instead, *Mycobacterium tuberculosis* MhuD transforms heme to iron and mycobilin,³ while *Staphylococcus aureus* IsdG and IsdI degrade heme to iron, staphylobilin, and formaldehyde.^{4,5} Recent reports strongly suggest that the first oxygenation reaction catalysed by MhuD⁶ and IsdG⁷ is the conversion of ferric-peroxoheme to *meso*-hydroxyheme, which is similar to the first oxygenation reaction catalysed by canonical HOs.⁸ However, based upon the active site structures, the mechanism of this reaction in canonical and non-canonical HOs must be different. In canonical HOs, an ordered network of water molecules is thought to guide a transient hydroxyl radical to the α -meso carbon of heme,^{9–11} but this ordered network of active site water molecules is absent in all available X-ray crystal structures of MhuD,^{12,13} IsdG,^{4,14,15} or IsdI.^{4,14–16} Several different research

groups have suggested that the novel reactivity of ferric-peroxoheme in non-canonical HOs is derived from the unique electronic structure of the heme substrate when bound by MhuD,¹³ IsdG,¹⁷ or IsdI.¹⁸

The ground state electron configurations of cyanide-inhibited MhuD (MhuD–heme–CN),¹³ IsdG (IsdG–heme–CN),¹⁷ and IsdI (IsdI–heme–CN)¹⁸ are distinct from those of cyanide-inhibited canonical HOs (HO–heme–CN),^{19–21} and population of this unique electronic state has been correlated with heme degradation activity.^{16,22} HO–heme–CN has the $(d_{xy})^2(d_{xz},d_{yz})^3$ ground state electron configuration that is typical for low-spin ferric heme,^{19–21} which will be referred to as a 2E_g state for the remainder of the article. In contrast, ^1H nuclear magnetic resonance (NMR) characterization of IsdI–heme–CN revealed that this species has a $(d_{xz},d_{yz})^4(d_{xy})^1$ ground state electron configuration that will be termed $^2B_{2g}$.¹⁸ The observation of a $^2B_{2g}$ state was exciting because previous work with model complexes had indicated that the $^2B_{2g}$ state has a strong electronic driving force to convert ferric-peroxoheme to *meso*-hydroxyheme, driven by large spin density on the *meso* carbons of the porphyrin ligand.²³ This possible explanation for the mechanism of the ferric-peroxoheme to *meso*-hydroxyheme reaction catalysed by non-canonical HOs was brought into question by the observation of “nested” variable-temperature, variable-field (VTVH) magnetic circular dichroism (MCD) saturation magnetization curves for MhuD–heme–CN (Fig. 1)¹³ and IsdG–heme–CN.¹⁷ These data clearly indicate that more than one $S = \frac{1}{2}$ state is populated at cryogenic temperatures, but how a single

Department of Chemistry, University of Vermont, Burlington, Vermont 05405, USA.

E-mail: matthew.liptak@uvm.edu

†Electronic supplementary information (ESI) available: Mutagenic primer sequences, gene sequences, UV CD data, and SDS-PAGE gels. See DOI: 10.1039/c6dt00702c

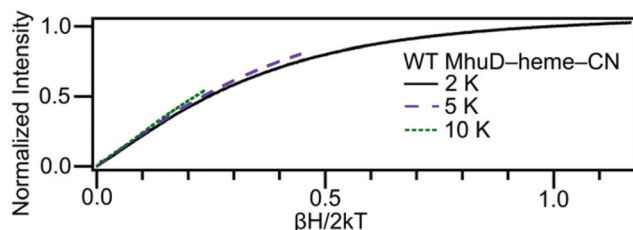


Fig. 1 VTVH MCD saturation magnetization curves for WT MhuD-heme-CN acquired at 2 (solid black line), 5 (dashed violet line), and 10 K (dotted green line).¹³ The curves are “nested”, which indicates that more than one electronic state is populated.

active site could have two or more degenerate electronic states has remained an open question without precedent. Since decreased out-of-plane distortion of the heme substrate in MhuD-heme-CN and IsdI-heme-CN has been shown to favour population of a 2E_g state, we hypothesize that the near degeneracy of the 2E_g and $^2B_{2g}$ states in non-canonical HOs is related to the out-of-plane distortion of the heme observed in all available X-ray crystal structures of non-canonical HOs.^{4,12–16}

Ruffling is the primary type of heme out-of-plane distortion observed in the X-ray crystal structures of MhuD,^{12,13} IsdG,^{4,14,15} and IsdI.^{4,14–16} This distortion has been defined as a deformation along the lowest energy b_{1u} normal mode of a porphyrin with idealized D_{4h} symmetry resulting in alternating clockwise and counter-clockwise rotation of the pyrrole rings about their Fe–N bonds.²⁴ The frequency of this vibrational mode is $<100\text{ cm}^{-1}$,²⁵ which means that it is important to consider both the average distortion of heme along this normal mode and the dynamic motion implied by its vibrational frequency. In MhuD-heme-CN and IsdI-heme-CN, the average distortion has been correlated to an electronic ground state change from 2E_g to $^2B_{2g}$.^{16,22} It is important to note that large ruffling deformations of heme have also been observed in model complexes where the driving force for ruffling cannot be steric interactions within a protein active site and must be electronic in origin.²⁶ Most likely, the electronic driving force for this ruffling deformation in model complexes is stabilization of a doubly-occupied orbital (porphyrin a_{2u}) at the expense of destabilizing a singly-occupied orbital (Fe $3d_{xy}$) resulting in an overall decrease of the electronic energy. In contrast, the electronic and functional implications of a dynamic ruffling motion of heme are less understood and will be the focus of this article.

This article reports the NMR and MCD spectroscopic characterization of F23A MhuD-heme-CN, F23W MhuD-heme-CN, and WT IsdI-heme-CN in addition to the development of a spectroscopically-validated *ab initio* model of the thermally-accessible electronic structure of cyanide-inhibited ferric heme. The polypeptide and substrate structures of the MhuD variants were assessed using circular dichroism (CD) and UV/Vis absorption (Abs) spectroscopies,²² respectively. ^1H nuclear magnetic resonance (NMR), MCD, and VTVH MCD were used to investigate the thermally-accessible electronic structures. The complete active space self-consistent field

(CASSCF) method was employed to model static correlation between the thermally-accessible electronic states of cyanide-inhibited ferric heme,²⁷ and N-electron valence state perturbation theory (NEVPT2) was used to treat dynamic electron correlation.^{28–30} We discuss the implications of the electronic structure model developed here for MhuD-, IsdG-, and IsdI-catalysed heme degradation.

Experimental

Unless otherwise noted, all materials used in this work were purchased from Fisher Scientific and used without further purification.

Protein expression and purification

The cloning of WT MhuD into pET-22b (Amp^r, Novagen) and S219V tobacco etch virus (TEV) protease into pRK793 (Amp^r), has been previously described.^{12,31} The F23A and F23W variants were prepared using the QuikChange Lightning site-directed mutagenesis kit. The DNA primers used for mutagenesis were purchased from the Midland Certified Reagent Company (Tables S1 and S2†). The pET-15b plasmid (Amp^r, Novagen) encoding WT IsdI was a gift from Eric Skaar (Vanderbilt University). DNA sequencing performed by the University of Vermont Cancer Center DNA Analysis facility confirmed the introduction of the F23A and F23W mutations into the pET-22b plasmid (Tables S3 and S4†), and retention of the WT IsdI gene in the pET-15b plasmid (Table S5†). Prior to expression and purification, plasmids encoding F23A MhuD, F23W MhuD, and WT IsdI were transformed into BL21-GOLD (DE3) cells (Stratagene).

WT MhuD was expressed and purified as previously reported.¹³ F23A and F23W MhuD were expressed as previously reported for WT enzyme. F23A and F23W cell pellets were lysed *via* sonication in 50 mM Tris pH 7.4, 50 mM NaCl, followed by centrifugation at 15 000g for 60 min at 4 °C. The filtered supernatant was loaded onto a HisPur Ni-NTA column (Pierce) equilibrated with 50 mM Tris pH 7.4, 50 mM NaCl. Following washes with: 50 mM Tris pH 7.4, 50 mM NaCl, 25 mM imidazole; 50 mM Tris pH 7.4, 50 mM NaCl, 50 mM imidazole; 50 mM Tris pH 7.4, 50 mM NaCl, 75 mM imidazole; and 50 mM Tris pH 7.4, 50 mM NaCl, 100 mM imidazole, F23A and F23W MhuD were eluted with 50 mM Tris pH 7.4, 50 mM NaCl, 400 mM imidazole. Using this procedure, F23A and F23W MhuD were obtained in >95% purity as determined by SDS-PAGE gel electrophoresis (Fig. S1 and S2†).

WT IsdI was expressed as previously reported.³² WT IsdI cell pellets were resuspended in 50 mM Tris pH 7.4, 150 mM NaCl, 100 μM phenylmethanesulfonyl fluoride (Pierce) with 10 units DNase1 (Pierce). Cells were lysed enzymatically by incubation with 1 mg mL^{−1} lysozyme for 1 h at 37 °C, followed by centrifugation at 15 000g for 1 h at 4 °C. The filtered supernatant was loaded onto a HisPur Ni-NTA column equilibrated with 50 mM Tris pH 7.4. Following washes with 50 mM Tris pH 7.4, 10 mM imidazole and 50 mM Tris pH 7.4, 150 mM NaCl, 50 mM imid-

azole; His₆-tagged IsdI was eluted with 50 mM Tris pH 7.4, 300 mM NaCl, 250 mM imidazole. The purified, His₆-tagged IsdI was dialyzed twice against 50 mM Tris pH 7.4 at 4 °C. Using this procedure, His₆-tagged IsdI was obtained with >99% purity as determined by SDS-PAGE gel electrophoresis (Fig. S3†).

S219V TEV protease was expressed and purified as described previously.¹⁷ S219V TEV protease was added to His₆-tagged IsdI in an OD₂₈₀ ratio of 1:10 along with sufficient dithiothreitol and ethyldiaminetetraacetic acid to reach final concentrations of 1 mM and 0.5 mM, respectively.³³ The mixture was incubated overnight at 4 °C, and then dialyzed twice against 50 mM Tris pH 7.4 at 4 °C. The dialyzed mixture was loaded onto a HisPur Ni-NTA column equilibrated with 50 mM Tris pH 7.4. Untagged IsdI was eluted with 50 mM Tris pH 7.4, and the eluate was re-loaded onto the Ni-NTA column and re-eluted two additional times. Using this procedure, untagged IsdI was obtained with >95% purity as determined by SDS-PAGE gel electrophoresis (Fig. S4†).

Spectroscopic characterization

WT MhuD-heme-CN, F23A MhuD-heme-CN, F23W MhuD-heme-CN, and WT IsdI-heme-CN were prepared as previously described for WT MhuD-heme-CN.¹³ The extinction coefficients for the Soret bands of F23A MhuD-heme-CN, F23W MhuD-heme-CN, and WT IsdI-heme-CN were determined using the pyridine hemochrome assay according to the procedure reported for WT MhuD-heme-CN.^{13,34} Room temperature Abs spectra were acquired for MhuD-heme-CN and IsdI-heme-CN samples in 50 mM Tris pH 7.4, 50 mM NaCl on a Cary 100 Bio spectrophotometer with a scan rate of 600 nm min⁻¹, a bandwidth of 2 nm, an averaging time of 0.1 s, and a data interval of 1 nm as described previously for W66F and W66A MhuD-heme-CN.²² ¹H NMR spectra of F23A and F23W MhuD-heme-CN samples in 20 mM sodium phosphate (NaPi) pH 7.4 were acquired at 25 °C using a Super-WEFT pulse sequence with a 50 ms τ -delay as previously described for WT MhuD-heme-CN.^{35,36}

A sample of F23W MhuD-heme-CN in 50 mM potassium phosphate (KP_i) pH 7.4, 50 mM NaCl, 60% (v/v) glycerol for cryogenic temperature MCD spectroscopic characterization was prepared as described previously for WT MhuD-heme-CN.¹³ An F23A MhuD-heme-CN sample for MCD spectroscopy was prepared by adding enough sucrose to a sample of F23A MhuD-heme-CN in 50 mM KP_i pH 7.4, 50 mM NaCl to form a saturated sucrose solution. The resulting mixture was incubated at 4 °C for 12 h, and then the supernatant was loaded into an oxygen-free copper/quartz sample cell and flash frozen in liquid nitrogen. A sample of WT IsdI-heme-CN in 50 mM KP_i pH 7.4, 60% (v/v) glycerol for MCD data collection was prepared as described previously for WT IsdG-heme-CN.¹⁷ 5 K MCD spectra, as well as VTVH MCD saturation magnetization curves, were acquired on an MCD setup consisting of a Jasco J-815 spectropolarimeter and an Oxford SM4000-8T Spectromag controlled by a Mercury iTC temperature controller and a Mercury iPS power supply. Spectral data was acquired with a scanning speed of 200 nm min⁻¹, a bandwidth of 1 nm, a

digital integration time of 0.2 s, and a data pitch of 0.5 nm. VTVH MCD saturation magnetization curves were measured at 2, 5, and 10 K for the 423 nm, 426 nm, and 437 nm peaks of F23A MhuD-heme-CN, F23W MhuD-heme-CN, and WT IsdI-heme-CN, respectively, using a magnetic field ramp rate of 0.7 T min⁻¹, a bandwidth of 1 nm, a digital integration time of 0.25 s, and a data pitch of 0.5 s. For all MCD data presented in this work, the natural CD contribution was removed from the MCD spectrum by subtracting the negative field data from the positive field data and dividing by 2.

CASSCF calculations

The generation of 36 structural models for cyanide-inhibited, His-ligated ferric heme with varying degrees of porphyrin ruffling using the PBE density functional and the TZVP basis set has been described previously (Fig. S5†).^{22,37,38} Quasi-restricted orbital (QRO) analyses of the ground state electronic structures,³⁹ and time-dependent DFT (TDDFT) predictions of the excited state electronic structures, have also been described previously.

For all 36 models, CASSCF calculations were performed using the TZVP basis set and tight SCF convergence criteria as implemented within the ORCA 3.0.0 software package on the 380 node IBM Bluemoon cluster maintained by the Vermont Advanced Computing Core.^{27,38,40} A state-averaged CASSCF calculation was employed to predict the three lowest-energy doublet states of a CAS(9,8) active space constructed from a PBE/TZVP QRO initial guess.²² The RIJCOSX method,⁴¹ in conjunction with the TZV/J and TZV/C auxiliary basis sets,^{42,43} was used to speed up calculation of the Coulomb and exchange terms, and the RI-MO algorithm was used to complete the CASSCF integral transformations. Finally, the NEVPT2 method was employed to predict the influence of dynamic electron correlation on the CASSCF state energies using a multi-reference perturbation theory approach.^{28–30}

Following CASSCF convergence, all active space orbitals were plotted in gOpenMol using isodensity values of ± 0.03 a.u. to assess whether the active orbitals were similar to the initial guess.^{44,45} In all cases, the active space consisted of the Fe 3d_{xy}, 3d_{xz}, 3d_{yz}, and 3d_{x²-y²} orbitals, in addition to the porphyrin 3a_{2u}, 1a_{1u}, and 4e_g* orbitals. Also, in all cases, the CASSCF orbital occupations for each active space orbital ranged from 0.06 to 1.94 electrons. For structural models where a (a_{2u})²(a_{1u})²(d_{xz})²(d_{yz})²(d_{xy})¹ electron configuration represented over 50% of the multi-configurational wavefunction for one state, this state was labelled ²B_{2g} and the other two states were labelled ²E_g. In all other cases, two states had 25–50% contributions from a (a_{2u})²(a_{1u})²(d_{xz})²(d_{yz})²(d_{xy})¹ configuration, and these two states were labelled ²B_{2g} + ²E_g, while the third state was labelled ²E_g.

Results

Spectroscopic characterization

The degree of porphyrin ruffling in F23A and F23W MhuD-heme-CN was assessed using UV/Vis Abs spectroscopy. This

approach was unnecessary for WT MhuD-heme-CN and IsdI-heme-CN since X-ray crystallography,^{13,18} and normal-coordinate structural decomposition analysis,²⁴ have demonstrated that the heme substrate has 1.4 Å and 2.3 Å of ruffling in these species, respectively. Previous research has established that ruffling distortions of up to 1.0 Å have no influence on the Q band energy, but trigger a blue-shift of the Soret band for cyanide-inhibited ferric heme.²² Beyond 1.0 Å, further ruffling red-shifts both the Q and Soret bands. The F23A substitution blue-shifts both the Q and Soret bands of MhuD-heme-CN from 18 100 cm⁻¹ to 18 500 cm⁻¹, and 23 900 cm⁻¹ to 24 000 cm⁻¹, respectively (Fig. 2). In contrast, the F23W substitution has no influence on the energy of the Soret band, and induces a slight red-shift of the Q band. When interpreted within the theoretical framework described above, the Abs data strongly suggests that the F23A substitution significantly alters electrostatic interactions between heme and the MhuD active site, while the spectral changes observed for F23W MhuD-heme-CN indicate a slight increase in porphyrin ruffling compared to WT enzyme. In order to ascertain whether these Abs spectral changes arose from polypeptide structural changes or relatively small perturbations of the active site structure, UV CD spectra were collected and analysed for samples of F23A and F23W MhuD-heme-CN (Fig. S6 and Table S6†). The data strongly suggests that the F23A or F23W substitutions do not trigger a significant change of the protein fold, meaning that the Abs spectral changes observed here can be attributed to small geometric rearrangements in the enzyme active site. Following Abs spectroscopic characterization, ¹H NMR spectroscopy was employed to investigate the influence of the F23A and F23W substitutions on the MhuD-heme-CN ground state electronic structure.

¹H NMR spectroscopic characterizations of the F23A and F23W variants indicate that these amino acid substitutions significantly alter the thermally-accessible electronic structure of MhuD-heme-CN. Previous studies strongly suggest that the ²E_g state of cyanide-inhibited heme oxygenases is associated with downfield hyperfine-shifted ¹H resonances,^{16,19–22} and ²B_{2g} states are associated with upfield hyperfine-shifted resonances.^{13,18} In WT MhuD-heme-CN, both downfield and

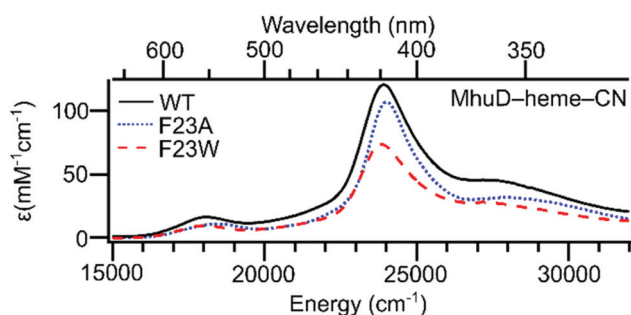


Fig. 2 Abs spectra of WT (solid black),¹³ F23A (dotted blue), and F23W (dashed red) MhuD-heme-CN in 50 mM Tris pH 7.4, 50 mM NaCl. The F23A substitution significantly alters the MhuD active site, while the F23W substitution increases porphyrin ruffling.

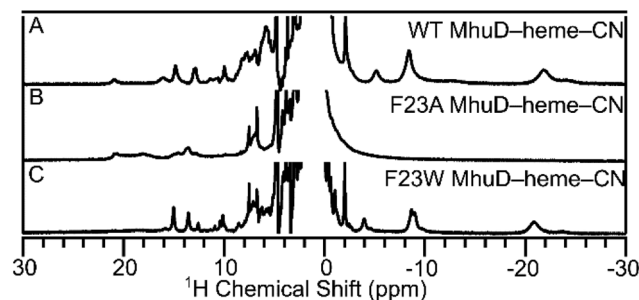


Fig. 3 ¹H NMR spectra of WT (panel A),¹³ F23A (panel B), and F23W (panel C) MhuD-heme-CN in 20 mM NaPi, pH 7.4, 50 mM NaCl recorded using a Super-WEFT pulse sequence. These data are consistent with a ²B_{2g} electronic ground state for WT and F23W MhuD-heme-CN, and a ²E_g ground state for the F23A variant.

upfield hyperfine shifted ¹H resonances were observed, and the temperature-dependence of the hyperfine shifts did not follow the Curie law, which led to the conclusion that both ²E_g and ²B_{2g} states are in fast exchange at physiologically-relevant temperatures.¹³ Compared to the ¹H NMR spectrum of WT MhuD-heme-CN, all upfield hyperfine-shifted resonances are lost in the spectrum of the F23A variant, while the downfield hyperfine-shifted resonances are retained (Fig. 3). On the other hand, in F23W MhuD-heme-CN, the upfield hyperfine-shifted resonances are retained and the downfield resonances observed beyond +16 ppm in WT enzyme are lost. These observations strongly suggest that F23A MhuD-heme-CN has a ²E_g electronic ground state and F23W MhuD-heme-CN has a ²B_{2g} ground state, although it is impossible to rule out the possibility that critical ¹H resonances are unobserved due to exchange broadening. Due to these ambiguities inherent to the ¹H NMR spectrum of ferric heme, the electronic structures of F23A and F23W MhuD-heme-CN were further investigated using cryogenic temperature MCD spectroscopy.

Previous work by our group has demonstrated that cryogenic temperature MCD spectroscopy provides more insight into the electronic structure of heme oxygenases than ¹H NMR spectroscopy or room temperature MCD spectroscopy.^{13,17,22} Previous 5 K MCD characterization of WT, W66F, and W66A MhuD-heme-CN has also identified a positively-signed feature at 20 000 cm⁻¹ whose intensity increases with increasing ²E_g population. This 20 000 cm⁻¹ band is present in the 5 K MCD spectrum of F23A MhuD-heme-CN, but not in that of F23W MhuD-heme-CN, consistent with a ²E_g ground state for F23A MhuD-heme-CN and a ²B_{2g} ground state for F23W MhuD-heme-CN (Fig. 4A). Previous research has also demonstrated that there is a correlation between the MhuD-heme-CN electronic ground state and the 5 K MCD intensity of the Soret band. At 5 K, F23A MhuD-heme-CN exhibits a more intense MCD Soret band than WT enzyme, and F23W has a much less intense feature. This is consistent with a ²E_g ground state for F23A MhuD-heme-CN and a ²B_{2g} ground state for F23W MhuD-heme-CN because ²E_g states have a source of C-term MCD intensity that is unavailable to a ²B_{2g} state, namely, spin-

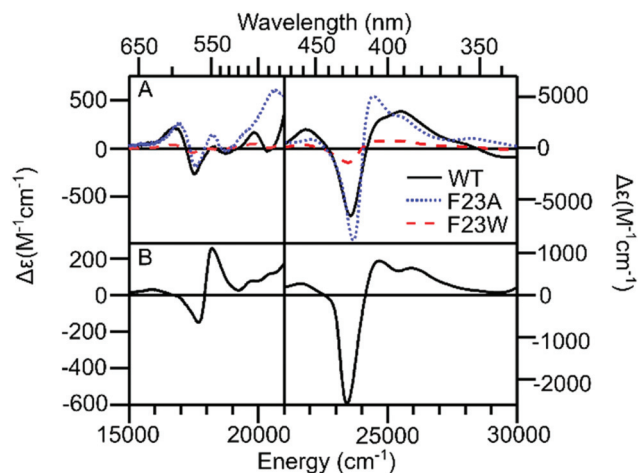


Fig. 4 5 K, 7 T MCD spectra of WT MhuD-heme-CN (solid black, panel A),¹³ F23A MhuD-heme-CN (dotted blue, panel A), F23W MhuD-heme-CN (dashed red, panel A), and WT IsdI-heme-CN (solid black, panel B). The MhuD-heme-CN data are consistent with 2E_g and $^2B_{2g}$ ground states for the F23A and F23W variants, respectively, while the data for IsdI-heme-CN suggests that more than one electronic state may be populated.

orbit coupling between the two orbital components of the 2E_g state.^{46,47} Considering the advantages of cryogenic temperature MCD spectroscopy compared to 1H NMR or room temperature MCD spectroscopy, cryogenic temperature MCD spectra of IsdI-heme-CN were collected in order to acquire data for a highly ruffled, crystallographically-characterized, heme oxygenase.

Somewhat surprisingly, the 5 K MCD spectrum of IsdI-heme-CN suggests that at least two electronic states are populated, despite the fact that no evidence for 2E_g population was observed in a previous 1H NMR and room temperature MCD characterization of the species.¹⁸ Although the room temperature MCD spectra of WT MhuD-heme-CN and IsdI-heme-CN are quite similar,¹³ the 5 K MCD spectra are significantly different demonstrating the enhanced sensitivity of cryogenic temperature MCD spectroscopy (Fig. 4B). These spectral differences can best be explained by the possibility that 5 K MCD spectroscopy can detect the electrostatic differences between the active site pockets of MhuD and IsdI. In support of this possibility, the 5 K MCD spectra of IsdI-heme-CN is very similar to that of IsdG-heme-CN,¹⁷ which has a nearly identical active site structure.¹⁴ Notably, the Soret band zero-crossing point in the IsdI-heme-CN MCD spectrum is blue-shifted by 300 cm^{-1} from $24\,100\text{ cm}^{-1}$ to $23\,800\text{ cm}^{-1}$ upon cooling the sample from room temperature to 5 K. The observation of a temperature-dependent Soret band energy in IsdI-heme-CN, which was previously observed for MhuD-heme-CN and attributed to the population of more than one electronic state, and the similarity of the IsdI-heme-CN 5 K MCD spectrum to that of IsdG-heme-CN, which has multiple thermally-accessible states, argues for the possibility that more than one electronic state may be populated in IsdI-heme-CN as well. Since VTVH

MCD spectroscopy has proven to provide the most conclusive evidence for the population of more than one $S = \frac{1}{2}$ state in heme oxygenases, VTVH MCD data was acquired for F23A and F23W MhuD-heme-CN, as well as WT IsdI-heme-CN.

VTVH MCD saturation magnetization curves were collected for the negatively-signed component of the F23A MhuD-heme-CN, F23W MhuD-heme-CN, and WT IsdI-heme-CN Soret bands because this band is known to be xy -polarized,⁴⁸ which means that the slope of saturation magnetization curve primarily depends upon the magnitude of g_z .⁴⁹ The 2 K, 5 K, and 10 K saturation magnetization curves for F23A MhuD-heme-CN overlay (Fig. 5A), suggesting that only one electronic state is populated in this variant. There is slight nesting of the VTVH saturation magnetization curves for F23W MhuD-heme-CN (Fig. 5B), which may suggest that F23W MhuD-heme-CN has a $^2B_{2g}$ ground state and a thermally-accessible 2E_g excited state. An overlay of the 2 K VTVH MCD saturation magnetization curves for WT, F23A, and F23W MhuD-heme-CN provides valuable insight into their electronic structures (Fig. 5C); the F23W variant has the largest population of $^2B_{2g}$ at 2 K and the F23A variant has the smallest population of $^2B_{2g}$. The WT IsdI-heme-CN VTVH MCD saturation magnetization curves are significantly “nested”, and their initial slope increases with increasing temperature (Fig. 5D). These data strongly suggest that the electronic ground state of IsdI-heme-CN is $^2B_{2g}$, as previously concluded based upon 1H NMR data,¹⁸ and a 2E_g state is thermally-accessible, as is the case for WT MhuD-heme-CN.¹³ With spectroscopic data now available for cyanide-inhibited ferric heme species whose porphyrin macrocycles are more ruffled than in WT MhuD-heme-CN, we turned our attention toward development of a multi-configurational computational model for cyanide-inhibited ferric heme.

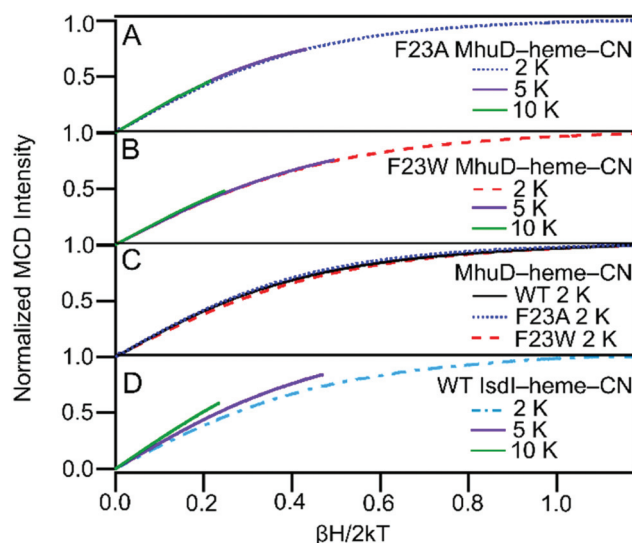


Fig. 5 VTVH MCD saturation magnetization curves for F23A MhuD-heme-CN (panel A), F23W MhuD-heme-CN (panel B), and WT IsdI-heme-CN (panel D) acquired at 2, 5, and 10 K. The 2 K curves for WT, F23A, and F23W MhuD-heme-CN are overlain in panel C.¹³

Computational analysis

Based upon the excellent agreement between PBE TDDFT-predicted porphyrin-based $\pi \rightarrow \pi^*$ transition energies for cyanide-inhibited ferric heme and experimental Abs spectra,²² the ability of PBE TDDFT to accurately model the thermally-accessible electronic structure of cyanide-inhibited ferric heme was tested. It is important to point out that, as a consequence of its formulation, PBE DFT includes an approximated treatment of dynamic electron correlation, but ignores static correlation arising from ground state near degeneracy in low-spin ferric heme.³⁷ In accordance with available ^1H NMR data for cyanide-inhibited HO and IsdI-heme-CN, PBE DFT correctly predicts a $^2\text{E}_g$ electronic ground state for the least ruffled model of cyanide-inhibited ferric heme, and a $^2\text{B}_{2g}$ ground state for the most ruffled model (Fig. 6A).^{18–21} However, at all degrees of ruffling, the predicted energy difference between the $^2\text{E}_g$ and $^2\text{B}_{2g}$ states is too large to account for the observation of multiple thermally-accessible electronic states in the VTVH MCD saturation magnetization curves of MhuD-heme-CN and IsdI-heme-CN.¹³ Furthermore, the noticeable discontinuities at 1.0 Å arise from rotation of the axial His from an orientation along an $\text{N}_{\text{pyr}}\text{--Fe--N}_{\text{pyr}}$ axis in less ruffled heme to an orientation along a $\text{C}_{\text{meso}}\text{--Fe--C}_{\text{meso}}$ axis in more ruffled heme consistent with adoption of an orientation that minimizes repulsion between the filled His π - and Fe 3d-based molecular orbitals of a $(d_{xy})^2(d_{xz},d_{yz})^3$ electron configuration below 1.0 Å and a $(d_{yz},d_{xz})^4(d_{xy})^1$ configuration above 1.0 Å. This raises the question as to whether the ruffling-induced electronic ground state change occurs at 1.9 Å as indicated by Löwdin orbital occupations or 1.0 Å as suggested by the molecular structure. Considering the clear shortcomings of PBE TDDFT with respect to the thermally-accessible electronic structure, CASSCF calculations were performed to incorporate static correlation.

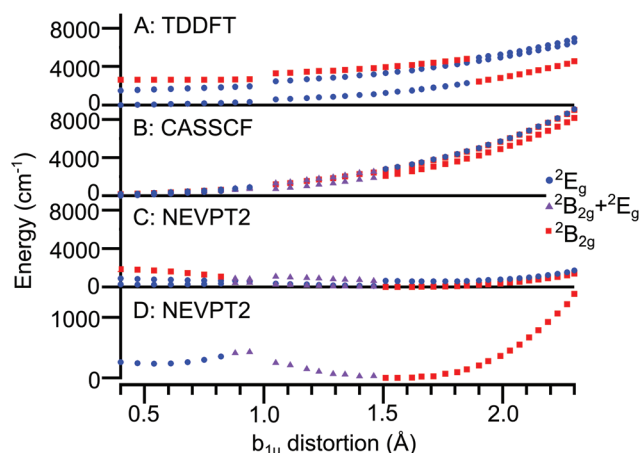


Fig. 6 $^2\text{E}_g$ (blue circles), $^2\text{B}_{2g}$ (red squares), and multi-configurational (violet triangles) state energies as a function of porphyrin ruffling, as predicted by TDDFT (panel A), CASSCF (panel B), and NEVPT2 (panel C) calculations. NEVPT2 predicts that a double well exists along the ruffling coordinate of the potential energy surface (panel D).

The CASSCF method incorporates static electron correlation by describing the electronic states as linear combinations of multiple electronic configurations.²⁷ A CAS(9,8) active space was employed because all eight active orbitals had occupations between 0.06 and 1.94 electrons (Fig. 7), and inclusion of the next closest energy set of orbitals, Fe $3d_{z^2}$ and porphyrin $2b_{1u}^*$, resulted in orbital occupations of less than 0.01 electrons. As was the case for DFT, the CASSCF-predicted electronic ground states for the least and most ruffled models are consistent with experimental data (Fig. 6B).^{18–21} However, unlike DFT, CASSCF predicts multi-configurational ground states for cyanide-inhibited ferric heme models with between 0.9 and 1.5 Å of porphyrin ruffling. Compared to TDDFT, the CASSCF-predicted energy difference between the $^2\text{E}_g$ and $^2\text{B}_{2g}$ states is an order of magnitude smaller, consistent with thermal population of electronic excited states in MhuD-heme-CN and IsdI-heme-CN.¹³ But, upon closer inspection, the energy difference between the states is predicted to increase with increased porphyrin ruffling, which is not consistent with the relative “nesting” behaviors of the VTVH MCD saturation magnetization curves for MhuD-heme-CN and IsdI-heme-CN. Since the remaining discrepancies between experiment and theory could be due to neglect of dynamic electron correlation by CASSCF, the NEVPT2 method was employed to model the effects of both static and dynamic electron correlation.

The NEVPT2 model is the most consistent with available experimental data of all the computational models tested here. NEVPT2 incorporates static electron correlation using an initial CASSCF step, and dynamic electron correlation with a second multi-reference perturbation theory step that is similar to the more popular CASPT2 method.^{28–30,50} As was the case for DFT and CASSCF, the NEVPT2-predicted electronic ground states for the least and most ruffled cyanide-inhibited ferric heme models are consistent with experiment (Fig. 6C).^{18–21} Unlike TDDFT or CASSCF, the NEVPT2-predicted energy difference between the $^2\text{E}_g$ and $^2\text{B}_{2g}$ electronic states is relatively large for small ruffling deformations and small for large ruffling deformations. This is significantly more consistent

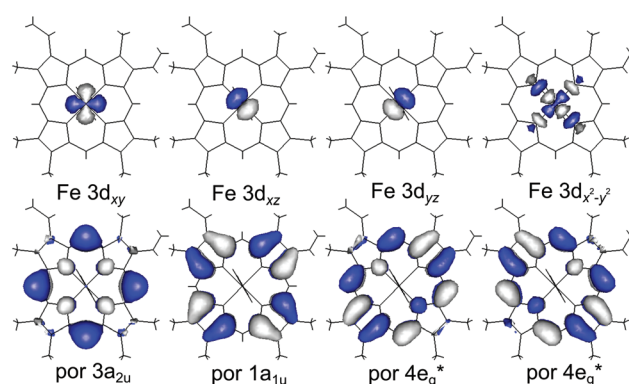


Fig. 7 Active space orbitals for the CASSCF and NEVPT2 calculations described here. All active space orbitals had occupations between 0.06 and 1.94 electrons.

with the VTVH MCD data for MhuD-heme-CN and IsdI-heme-CN than the energy differences predicted by TDDFT or CASSCF.¹³ A notable feature of the NEVPT2-predicted ground state potential energy surface of cyanide-inhibited ferric heme is the double-well along the ruffling coordinate (Fig. 6D), which arises from an avoided crossing of the 2E_g and $^2B_{2g}$ electronic states at 1.0 Å of ruffling. Overall, the NEVPT2 model provides the most accurate, comprehensive electronic structure model of cyanide-inhibited ferric heme reported to date.

Discussion

Structural implications of the double-well potential

The NEVPT2-predicted double-well potential on the ruffling coordinate of cyanide-inhibited ferric heme implies that two stable conformations of heme are available to heme oxygenases. The less ruffled conformation has an average ruffling distortion of 0.5 Å and a 2E_g electronic ground state, while the more ruffled conformation has an average distortion of 1.6 Å and a $^2B_{2g}$ ground state (Fig. 6).^{22,24} The two conformations are separated by a 1.2 kcal mol⁻¹ barrier, meaning that conformation exchange is facile, especially at physiologically-relevant temperatures. While the NEVPT2 model described here was developed for protein-free cyanide- and imidazole-ligated ferric heme due to the diverse library of spectroscopic data available, the findings are relevant for all forms of low-spin ferric heme. Altering the axial ligands will tune the Fe 3d orbital energies perturbing the minimum energy structures and relative energies of the 2E_g and $^2B_{2g}$ conformations, but there will still be two conformations and the more ruffled conformation will still have a $^2B_{2g}$ electronic ground state. To a lesser extent, second-sphere interactions between protein active sites and heme will also influence the average structures of and the relative energies of the two conformations. Nevertheless, this model was developed for cyanide-inhibited ferric heme and it is most appropriate to discuss how it explains a range of structural observations in the literature for MhuD-heme-CN and IsdI-heme-CN.

The X-ray crystal structures of diheme-bound (MhuD-diheme, PDB ID 3HX9),¹² MhuD-heme-CN (PDB ID 4NL5),¹³ and W66Y IsdI-heme-CN (PDB ID 4FNI)¹⁶ are consistent with the presence of two heme conformations when examined within the framework of the NEVPT2 potential energy surface. The solvent-exposed heme in the X-ray crystal structure of MhuD-diheme has 0.7 Å of ruffling, but 1.3 and 1.4 Å ruffled hemes were observed in the X-ray crystal structure of MhuD-heme-CN (Table 1).^{22,24} Evidence for the existence of two heme conformations can also be seen in the dimeric crystal structure of W66Y IsdI-heme-CN, where one polypeptide chain binds a heme with 1.9 Å of ruffling and the other with 1.5 Å of ruffling. Furthermore, structural alignment of the two chains of W66Y IsdI-heme-CN reveals that the only significant structural changes in the active site are the heme conformation and axial His orientation. The correlation between ruffling and His orientation, which has been noted pre-

Table 1 Ruffling distortions and axial his orientations

Structure	Ruffling ^a	His angle ^b
MhuD-diheme (A) ^c	0.7 Å	-24°
MhuD-diheme (B) ^c	0.7 Å	-26°
MhuD-heme-CN (A) ^d	1.3 Å	-10°
MhuD-heme-CN (B) ^d	1.4 Å	-10°
W66Y IsdI-heme-CN (A) ^e	1.9 Å	+10°
W66Y IsdI-heme-CN (B) ^e	1.5 Å	+24°

^a b_{1u} out-of-plane distortion as determined by normal-coordinate structural decomposition.^{22,24} ^b His(Cε)-His(Nε)-Fe-C(α-meso) angle phase-shifted to between -45° and +45°. ^c PDB ID 3HX9. ^d PDB ID 4NL5. ^e PDB ID 4FNI.¹⁶

viously,⁵¹ is also present in the MhuD-diheme, MhuD-heme-CN, and W66Y IsdI-heme-CN structures. The ruffling conformational change from MhuD-diheme to MhuD-heme-CN is accompanied by rotation of the axial His from an orientation mostly along the N_{pyr} -Fe- N_{pyr} axis to one more closely aligned with the C_{meso} -Fe- C_{meso} axis. The same pattern follows for W66Y IsdI-heme-CN, where the His bound to the less ruffled heme is oriented closer to the N_{pyr} -Fe- N_{pyr} axis and the His bound to the more ruffled heme is oriented along the C_{meso} -Fe- C_{meso} axis. As may be expected, the double-well potential energy surface has even more dramatic electronic implications for MhuD-heme-CN and IsdI-heme-CN.

Electronic implications of the double-well potential

The NEVPT2-predicted double-well potential for cyanide-inhibited ferric heme can explain all of the VTVH MCD data acquired for MhuD-heme-CN, cyanide-inhibited IsdG (IsdG-heme-CN), and IsdI-heme-CN to date. At cryogenic temperatures, thermal equilibrium is established between the less ruffled 2E_g conformation and the more ruffled $^2B_{2g}$ conformation, since the two conformations are only separated by 0.7 kcal mol⁻¹ in the absence of perturbations from the enzyme active site and no large scale structural rearrangements are required (Fig. 8). In WT MhuD-heme-CN, there exists a $^2B_{2g}$ ground state, with a shallow saturation magnetization curve, and a 2E_g excited state, with a steep saturation magnetization curve, which is populated by a variety of mechanisms, including: conformational exchange, thermal excitation, and spin-orbit coupling (Fig. 1).¹³ The VTVH MCD data for W66F, W66A, and F23W MhuD-heme-CN strongly suggest that second-sphere substitutions can perturb this potential energy surface by stabilizing either the 2E_g conformation, for W66F and W66A MhuD-heme-CN, or the $^2B_{2g}$ conformation, for F23W MhuD-heme-CN, since the saturation magnetization curves are less “nested” than those observed for WT enzyme (Fig. 5).²² The F23A MhuD-heme-CN Abs and VTVH MCD data demonstrate that it is possible to completely collapse the double-well potential into a single-well by significantly altering electrostatic interactions between heme and the enzyme active site. On the other hand, IsdG-heme-CN and IsdI-heme-CN have the most “nested” VTVH MCD saturation magnetization curves measured to date for cyanide-inhibited

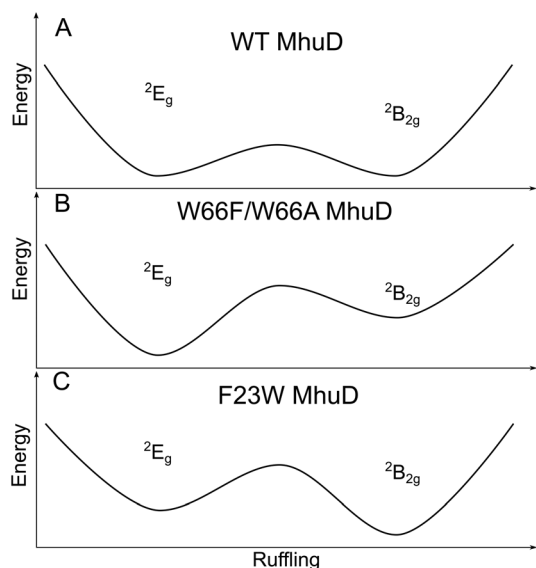


Fig. 8 The potential energy surface along the heme ruffling coordinate is broad and relatively flat in MhuD, IsdG, and IsdI. The native enzyme active sites are proposed to minimize the barrier between the two conformations (panel A), and second-sphere substitutions can stabilize either the less ruffled 2E_g conformation (panel B) or the more ruffled $^2B_{2g}$ conformation (panel C).

ferric heme,¹⁷ suggesting that these enzyme active sites may have evolved to maximally flatten the potential energy surface along the ruffling coordinate of the heme substrate. In addition to providing a satisfactory explanation for all of the VTVH MCD data acquired at cryogenic temperatures, the double-well potential also explains the ^1H NMR data acquired at physiologically-relevant temperatures.

The ^1H NMR data reported for MhuD-heme-CN, IsdI-heme-CN, and hydroxide-bound IsdI (IsdI-heme-OH) can be readily understood within the framework of the NEVPT2-predicted double-well potential. At physiologically-relevant temperatures, the rate of exchange between the less ruffled 2E_g conformation and the more ruffled $^2B_{2g}$ conformation will be fast on the NMR time-scale meaning that exchange broadened resonances will be observed at population-weighted average chemical shifts (Fig. 8). The ^1H NMR spectrum of WT MhuD-heme-CN has exchange broadened ^1H resonances consistent with population of both $^2B_{2g}$ and 2E_g states at 37 °C, and the temperature-dependence of the chemical shifts is consistent with thermal population of the 2E_g excited state.¹³ In IsdI-heme-CN, the enzyme active site strongly favors population of a $^2B_{2g}$ state, but exchange broadening is still evident in the ^1H NMR spectrum.¹⁸ Based upon ^1H NMR data, it is apparent that the W66F, W66A, and F23W variants of MhuD, and the W66F and W66Y variants of IsdI, can perturb the ruffling potential energy surface of cyanide-inhibited ferric heme in a way that favours one conformation over the other, but in all cases exchange broadening is still detected (Fig. 3).^{16,22} It is also important to point out that ^1H NMR evidence exists for

exchange broadening in IsdI-heme-OH, indicating that the dynamic exchange between the two ruffled conformations with different electronic ground states is not limited to cyanide-inhibited ferric heme. Thus, all available spectroscopic data strongly suggest that there is significant dynamic motion of the heme substrate and its axial His ligand between the idealized 2E_g and $^2B_{2g}$ conformations in the active sites of MhuD, IsdG, and IsdI.

Functional implications of the double-well potential

The dynamic ruffling motion of the heme substrate predicted by NEVPT2 calculations, and supported by spectroscopic data, has important implications for the heme degrading reactions catalysed by MhuD, IsdG, and IsdI. The dynamic motion means that the heme substrate will regularly and frequently achieve ruffling distortions that are significantly larger or smaller than those observed in X-ray crystal structures. The enhanced, instantaneous ruffling distortion will further favour the proposed bridged transition state mechanism for the first oxygenation step by bringing the *meso* carbons closer to a distal hydroperoxo ligand.^{17,52} Also, it is important to realize that the structural dynamics will be coupled to electron dynamics where electron density will shuttle between the Fe 3d orbitals and the porphyrin $3a_{2u}$ orbital as a consequence of the differences between the 2E_g and $^2B_{2g}$ electronic structures. Instantaneous structures with small ruffling distortions will favour $\text{Fe(III)} \rightarrow \text{Fe(II)}$ reduction since ruffling has been predicted to lower the reduction potential of heme.⁵³ Instantaneous structures with large ruffling distortions will favour nucleophilic attack of the *meso* carbons by depleting electron density in the porphyrin $3a_{2u}$ orbital.^{22,23} We propose here that the MhuD, IsdG, and IsdI active sites have evolved to maximize the ruffling dynamics of heme in order to catalyse the successive oxygenations of heme to mycobilin and staphylobilin by distinct mechanistic steps.^{3,4}

Conclusions

In summary, an accurate computational model of the thermally-accessible electronic structure of cyanide-inhibited ferric heme has been developed, and has a double-well potential along the out-of-plane ruffling coordinate of the porphyrin macrocycle. Development of an accurate model required a CASSCF treatment of static electron correlation and a NEVPT2 treatment of dynamic electron correlation. The NEVPT2-predicted double-well potential explains the unusual “nesting” of the VTVH MCD saturation magnetization curves for MhuD-heme-CN, IsdG-heme-CN, and IsdI-heme-CN. In addition, the small energy barrier between the two conformations explains the exchange broadened ^1H NMR resonances observed for MhuD and IsdI. Ultimately, these data imply that the heme substrate of MhuD, IsdG, and IsdI is dynamic, with both the degree of porphyrin ruffling and electron density distribution evolving over time.

Acknowledgements

M. D. L. thanks the *University of Vermont* for financial support. The authors thank Eric Skaar (Vanderbilt University) and Celia Goulding (University of California-Irvine) for the gift of the pET-15b plasmid encoding TEV-cleavable, His₆-tagged IsdI. The authors acknowledge the Vermont Advanced Computing Core which is supported by NASA (NNX-06AC88G), at the University of Vermont for providing High Performance Computing resources that have contributed to the results reported within this paper.

References

- 1 A. Wilks and M. Ikeda-Saito, *Acc. Chem. Res.*, 2014, **47**, 2291–2298.
- 2 A. Wilks and G. Heinzl, *Arch. Biochem. Biophys.*, 2014, **544**, 87–95.
- 3 S. Nambu, T. Matsui, C. W. Goulding, S. Takahashi and M. Ikeda-Saito, *J. Biol. Chem.*, 2013, **288**, 10101–10109.
- 4 M. L. Reniere, G. Ukpabi, S. R. Harry, D. F. Stec, R. Krull, D. W. Wright, B. O. Bachmann, M. E. P. Murphy and E. P. Skaar, *Mol. Microbiol.*, 2010, **75**, 1529–1538.
- 5 T. Matsui, S. Nambu, Y. Ono, C. W. Goulding, K. Tsumoto and M. Ikeda-Saito, *Biochemistry*, 2013, **52**, 3025–3027.
- 6 T. Matsui, S. Nambu, C. W. Goulding, S. Takahashi, H. Fujii and M. Ikeda-Saito, *Proc. Natl. Acad. Sci. U. S. A.*, 2016, **113**, 3779–3784.
- 7 B. R. Streit, R. Kant, M. Tokmina-Lukaszewska, A. I. Celis, M. M. Machovina, E. P. Skaar, B. Bothner and J. L. DuBois, *J. Biol. Chem.*, 2016, **291**, 862–871.
- 8 Y. Liu, P. Moënne-Loccoz, T. M. Loehr and P. R. Ortiz de Montellano, *J. Biol. Chem.*, 1997, **272**, 6909–6917.
- 9 R. T. Syvitski, Y. Li, K. Auclair, P. R. Ortiz de Montellano and G. N. La Mar, *J. Am. Chem. Soc.*, 2002, **124**, 14296–14297.
- 10 R. Garcia-Serres, R. M. Davydov, T. Matsui, M. Ikeda-Saito, B. M. Hoffman and B. H. Huynh, *J. Am. Chem. Soc.*, 2007, **129**, 1402–1417.
- 11 H. Chen, Y. Moreau, E. Derat and S. Shaik, *J. Am. Chem. Soc.*, 2008, **130**, 1953–1965.
- 12 N. Chim, A. Iniguez, T. Q. Nguyen and C. W. Goulding, *J. Mol. Biol.*, 2010, **395**, 595–608.
- 13 A. B. Graves, R. P. Morse, A. Chao, A. Iniguez, C. W. Goulding and M. D. Liptak, *Inorg. Chem.*, 2014, **53**, 5931–5940.
- 14 R. Wu, E. P. Skaar, R. Zhang, G. Joachmiak, P. Gornicki, O. Schneewind and A. Joachmiak, *J. Biol. Chem.*, 2005, **280**, 2840–2846.
- 15 W. C. Lee, M. L. Reniere, E. P. Skaar and M. E. Murphy, *J. Biol. Chem.*, 2008, **283**, 30957–30963.
- 16 G. Ukpabi, S. J. Takayama, A. G. Mauk and M. E. Murphy, *J. Biol. Chem.*, 2012, **287**, 34179–34188.
- 17 C. L. Lockhart, M. A. Conger, D. S. Pittman and M. D. Liptak, *J. Biol. Inorg. Chem.*, 2015, **20**, 757–770.
- 18 S. J. Takayama, G. Ukpabi, M. E. Murphy and A. G. Mauk, *Proc. Natl. Acad. Sci. U. S. A.*, 2011, **108**, 13071–13076.
- 19 C. M. Gorst, A. Wilks, D. C. Yeh, P. R. Ortiz de Montellano and G. N. La Mar, *J. Am. Chem. Soc.*, 1998, **120**, 8875–8884.
- 20 G. A. Caignan, R. Deshmukh, A. Wilks, Y. Zeng, H. Huang, P. Moënne-Loccoz, R. A. Bunce, M. A. Eastman and M. Rivera, *J. Am. Chem. Soc.*, 2002, **124**, 14879–14892.
- 21 H. Ogura, J. P. Evans, D. Peng, J. D. Satterlee, P. R. Ortiz de Montellano and G. N. La Mar, *Biochemistry*, 2009, **48**, 3127–3137.
- 22 A. B. Graves, M. T. Graves and M. D. Liptak, *J. Phys. Chem. B*, 2016, **120**, 3844–3853.
- 23 M. Rivera, G. A. Caignan, A. V. Astashkin, A. M. Raitsimring, T. K. Shokhireva and F. A. Walker, *J. Am. Chem. Soc.*, 2002, **124**, 6077–6089.
- 24 W. Jentzen, X.-Z. Song and J. A. Shelnutt, *J. Phys. Chem. B*, 1997, **101**, 1684–1699.
- 25 M. Kubo, F. Gruia, A. Benabbas, A. Barabanschikov, W. R. Montfort, E. M. Maes and P. M. Champion, *J. Am. Chem. Soc.*, 2008, **130**, 9800–9811.
- 26 M. Nakamura, *Coord. Chem. Rev.*, 2006, **250**, 2271–2294.
- 27 B. O. Roos, P. R. Taylor and P. E. M. Siegbahn, *Chem. Phys.*, 1980, **48**, 157–173.
- 28 C. Angeli, R. Cimiraglia, S. Evangelisti, T. Leininger and J.-P. Malrieu, *J. Chem. Phys.*, 2001, **114**, 10252–10264.
- 29 C. Angeli, R. Cimiraglia and J.-P. Malrieu, *Chem. Phys. Lett.*, 2001, **350**, 297–305.
- 30 C. Angeli, R. Cimiraglia and J.-P. Malrieu, *J. Chem. Phys.*, 2002, **117**, 9138–9153.
- 31 R. B. Kapust, J. Tözsér, J. D. Fox, D. E. Anderson, S. Cherry, T. D. Copeland and D. S. Waugh, *Protein Eng.*, 2001, **14**, 993–1000.
- 32 E. P. Skaar, A. H. Gaspar and O. Schneewind, *J. Biol. Chem.*, 2004, **279**, 436–443.
- 33 S. Nallamsetty, R. B. Kapust, J. Tözsér, S. Cherry, J. E. Tropea, T. D. Copeland and D. S. Waugh, *Protein Expression Purif.*, 2004, **37**, 108–115.
- 34 E. A. Berry and B. L. Trumpower, *Anal. Biochem.*, 1987, **161**, 1–15.
- 35 S. L. Patt and B. D. Sykes, *J. Chem. Phys.*, 1972, **56**, 3182–3184.
- 36 T. Inubushi and E. D. Becker, *J. Magn. Reson.*, 1983, **51**, 128–133.
- 37 J. P. Perdew, K. Burke and M. Ernzerhof, *Phys. Rev. Lett.*, 1996, **77**, 3865–3868.
- 38 A. Schäfer, H. Horn and R. Ahlrichs, *J. Chem. Phys.*, 1992, **97**, 2571–2577.
- 39 F. Neese, *J. Am. Chem. Soc.*, 2006, **128**, 10213–10222.
- 40 F. Neese, *Wiley Interdiscip. Rev.: Comput. Mol. Sci.*, 2012, **2**, 73–78.
- 41 R. Izsák and F. Neese, *J. Chem. Phys.*, 2011, **135**, 144105.
- 42 K. Eichkorn, F. Weigend, O. Treutler and R. Ahlrichs, *Theor. Chem. Acc.*, 1997, **97**, 119–124.
- 43 F. Weigend, M. Häser, H. Patzelt and R. Ahlrichs, *Chem. Phys. Lett.*, 1998, **294**, 143–152.
- 44 A. Laaksonen, *J. Mol. Graphics*, 1992, **10**, 33–34.

- 45 D. L. Bergman, L. Laaksonen and A. Laaksonen, *J. Mol. Graphics*, 1997, **15**, 301–306.
- 46 M. R. Cheesman and F. A. Walker, *J. Am. Chem. Soc.*, 1996, **118**, 7373–7380.
- 47 N. Lehnert, *J. Inorg. Biochem.*, 2012, **110**, 83–93.
- 48 M. Gouterman, *J. Chem. Phys.*, 1959, **30**, 1139–1161.
- 49 F. Neese and E. I. Solomon, *Inorg. Chem.*, 1999, **38**, 1847–1865.
- 50 K. Andersson, P.-A. Malmqvist, B. O. Roos, A. J. Sadlej and K. Wolinski, *J. Phys. Chem.*, 1990, **94**, 5483–5488.
- 51 F. A. Walker, *Coord. Chem. Rev.*, 1999, **185–186**, 471–534.
- 52 S. J. Takayama, S. A. Loutet, A. G. Mauk and M. E. Murphy, *Biochemistry*, 2015, **54**, 2613–2621.
- 53 M. D. Liptak, X. Wen and K. L. Bren, *J. Am. Chem. Soc.*, 2010, **132**, 9753–9763.